



Compositional effects in the liquid Fe–Ni–C system at high pressure

Esther S. Posner¹ · Gerd Steinle-Neumann¹

Received: 11 January 2022 / Accepted: 5 October 2022 / Published online: 27 October 2022
© The Author(s) 2022

Abstract

We performed molecular dynamics simulations based on density functional theory to systematically investigate the Fe–Ni–C system including (1) pure Fe and Ni; (2) binary Fe–Ni, Fe–C, and Ni–C; and (3) ternary Fe–Ni–C liquid compositions at 3000 K and three simulation volumes corresponding to pressure (P) up to 83 GPa. Liquid structural properties, including coordination numbers, are analyzed using partial radial distribution functions. Self-diffusion coefficients are determined based on the atomic trajectories and the asymptotic slope of the time-dependent mean-square displacement. The results indicate that the average interatomic distance between two Fe atoms ($r_{\text{Fe-Fe}}$) decreases with P and is sensitive to Ni (X_{Ni}) and C (X_{C}) concentration, although the effects are opposite: $r_{\text{Fe-Fe}}$ decreases with increasing X_{Ni} , but increases with increasing X_{C} . Average $r_{\text{Fe-C}}$ and $r_{\text{Ni-C}}$ values also decrease with increasing X_{Ni} and generally remain constant between the two lowest P points, corresponding to a coordination change of carbon from ~ 6.8 to ~ 8.0 , and then decrease with additional P once the coordination change is complete. Carbon clustering occurs in both binary (especially Ni–C) and ternary compositions with short-range $r_{\text{C-C}}$ values (~ 1.29 to ~ 1.57 Å), typical for $r_{\text{C-C}}$ in diamond and graphite. The self-diffusion results are generally consistent with high- P diffusion data extrapolated from experiments conducted at lower temperature (T). A subset of additional simulations was conducted at 1675 and 2350 K to estimate the effect of T on diffusion, yielding an activation enthalpy of ~ 53 kJ/mol and activation volume of ~ 0.5 cm³/mol.

Keywords Liquid iron alloys · Nickel · Carbon · High pressure · Compositional effect · Core formation

Introduction

The cores of the Earth and terrestrial planets (Mercury, Venus, Mars, and the Moon) are composed of multi-component Fe–Ni alloys with substantial concentrations of at least one light element (LE) (e.g., S, O, Si, C, N, H) (e.g., Hirose et al. 2021). In this context, the partitioning behavior of an element between Fe-rich metal and silicate melt is a critical parameter for constraining the chemical and physical differentiation of core and mantle during planetary formation. Nickel has a larger metal-silicate partition coefficient than Fe (e.g., Corgne et al. 2008; Fischer et al. 2015) and is thus consistently found in iron meteorites, its concentration ranging from approximately 4.3 wt.% to as high as 34 wt.% (e.g., Vander Voort 2001) with the proportion increasing

with decreasing oxygen fugacity (e.g., Benedix et al. 2014; Corgne et al. 2008).

The geoscience community has traditionally considered Ni to be the “geochemical twin” of Fe owing largely to their similar atomic mass and radius (e.g., Wells 1984), and Ni has therefore been frequently excluded from studies in mineral physics to minimize the complexity of both experiments and computational work on core analog materials. However, the appropriateness of this simplifying assumption is debatable: (1) the steelmaking industry has extensively documented the non-negligible influence of Ni on the properties of commercial steel (e.g., Knowles 1987; Keehan et al. 2006), particularly in terms of yield strength, hardness, and hardenability; (2) even in the binary liquid at ambient pressure (P), Fe and Ni have been shown to not mix ideally, with some excess volume measured (Watanabe et al. 2016); and (3) several geochemical studies have shown that the presence of Ni reduces the solubility of several elements (e.g., C, Re, Ir) in liquid Fe, and enhances that of others (e.g., S, Sn) (e.g., Tsymbulov and Tsemekhman 2001; Fonseca et al. 2011; Capobiano et al., 1999). Furthermore, Ni has

✉ Esther S. Posner
esther.posner@uni-bayreuth.de

¹ Bayerisches Geoinstitut, Universität Bayreuth,
95440 Bayreuth, Germany

been suggested to potentially affect the diffusion coefficient (D) of carbon in liquid Fe alloys based on a comparison of carbon diffusion data determined from high- P experiments in liquid Fe–C (Rebaza et al. 2021; Dobson and Wiedenbeck 2002) and simulations on liquid Fe–Ni–C (Wang et al. 2019). While previous studies have directly verified the effect of Ni on the material and geochemical equilibrium properties of Fe alloys relative to Ni-free compositions, as mentioned above, the influence of Ni on the transport properties of liquid Fe–LE alloys has not been investigated. In fact, Ni has been excluded from all experimental diffusion studies involving liquid iron alloys at high- P , which presently remain limited to pure liquid Fe (Dobson 2002) and binary alloys, Fe–S (Dobson 2000), Fe–O (Posner et al. 2017a), Fe–C (Rebaza et al. 2021; Dobson and Wiedenbeck 2002), Fe–Si, and Fe–Cr (Posner et al. 2017b).

Because Ni is expected to be present in the core of the Earth and other terrestrial planets, a comprehensive understanding of its influence on the properties of liquid Fe alloys is of great significance. Liquid metal transport properties (e.g., diffusion, viscosity) are crucial parameters for constraining the kinetics of mass exchange and extent of chemical equilibrium between core-forming metals and silicate melt during core formation in a magma ocean (e.g., Rubie et al. 2003, 2015), as well as ongoing reactions across the core-mantle boundary (e.g., Jeanloz 1990; Knittle and Jeanloz 1991) including the formation and stability of a light-element enriched layer at the top of the core (e.g., Gubbins and Davies 2013). A direct comparison of the experimental diffusion data in liquid Fe–C by Rebaza et al. (2021) and Dobson and Wiedenbeck (2002) with the computational results on Fe–Ni–C by Wang et al. (2019) is not possible largely because (1) the computational study was conducted at a single temperature (T), several hundred K lower than the experiments and possibly below the melting point for $P > 10$ GPa (e.g., Mashino et al. 2019); (2) the T dependence of D_C in liquid Fe–Ni–C required for extrapolation is unknown; and (3) the C concentrations vary between the different studies (~ 10 –25 at.%), which has been shown to influence D_C in carbon steel (e.g., Liu et al. 1991). Furthermore, Dobson and Wiedenbeck (2002) reported a relatively strong effect of P on D_C , whereas the C diffusion data of Rebaza et al. (2021) showed a practically negligible P effect, which they attributed to differing C contents but did not test.

To systematically address this question, we investigated the Fe–Ni–C system at 3000 K using density functional theory (DFT) based molecular dynamics (MD) simulations on (1) pure liquid Fe and Ni; (2) binary Fe–Ni, Fe–C, and Ni–C; and (3) ternary Fe–Ni–C compositions. The Ni (X_{Ni})

and C (X_C) contents were varied between 1 and 90 at% and 1 and 20 at%, respectively. Three simulation volumes were set up to determine the effect of P on each composition, and a subset of simulations were run at 1675 and 2350 K to determine the effect of T .

Methods

Molecular dynamics simulations were performed in the canonical (N - V - T) ensemble within Kohn-Sham DFT to compute the electronic structure of the liquid. The Vienna ab initio simulation package (Kresse and Furthmüller 1996) was used to calculate total energy and Hellmann-Feynman forces. The electronic density at each simulation step was determined by the projector augmented wave formalism (Kresse and Joubert 1999) with the generalized gradient approximation to exchange and correlation (Perdew et al. 1996).

Following our previous studies (Posner et al. 2017a, c; Posner and Steinle-Neumann 2019), non-spin-polarized simulations were performed for cells with 150 atoms, reciprocal space was sampled only at the Γ -point, and wave functions were expanded into plane waves with a cutoff energy of 550 eV. Cells were initially set up based on pure Fe configurations that were overheated and Fe atoms were then replaced by Ni or C in proportions listed in Table SM1 of the Supplemental Material. We consider three cell volumes V_x ($7.121 \text{ cm}^3/\text{mol} = 1173 \text{ \AA}^3/\text{cell}$), $0.9V_x$, and $0.8V_x$ for all compositions. For the high-carbon (20 at%) compositions, runs at V_x were replaced with $0.7V_x$ because the V_x simulations yielded negative P values from the evaluation of the Hellmann-Feynman stress tensor (i.e., < 0 GPa). Simulations were conducted at $T = 3000$ K using a Nosé-Hoover thermostat (Anderson 1980). Additional simulations were conducted at $T = 1675$ and 2350 K using the same composition as that reported by Wang et al. (2019) (Fe–7%Ni–20%C) for the following reasons: (1) to explore whether structures accessed at 1675 K represent a liquid despite being below the melting curve; (2) to see whether we reproduce the spin-polarized results by Wang et al. (2019) by our non-spin-polarized simulations; and (3) to determine the T dependence of diffusivities. To further test whether spin-polarized and spin-degenerate simulations yield equivalent results, we performed and analyzed one run for Fe–50%Ni–20%C at low P , and found that results do not differ in any significant way, despite the existence of magnetic moments on the Fe and Ni atoms. All simulations were run for at least 29 ps

with a time step of 1 fs, and the first 2 ps were discarded to allow for equilibration.

Structural properties were investigated by analyzing the partial radial distribution functions (RDFs), namely, $g_{\text{Fe-Fe}}(r)$, $g_{\text{Fe-Ni}}(r)$, $g_{\text{Fe-C}}(r)$, $g_{\text{Ni-Ni}}(r)$, $g_{\text{Ni-C}}(r)$, and $g_{\text{C-C}}(r)$ and the corresponding partial and total coordination numbers. Considering an atom of species a , the probability of finding an atom of species b in a spherical shell ($r, r + dr$) is defined as:

$$g_{a-b}(r) = 4\pi r^2 \rho_b g_{a-b}(r) dr, \tag{1}$$

where $\rho_b = X_b/V$ is the number density of species b with a mole fraction X_b and V is the volume per atom. The coordination number N_{a-b} represents the average number of nearest neighbors of species b surrounding an atom of species a and is calculated as

$$N_{a-b} = 4\pi \rho_b \int_0^{r_{a-b}} r^2 g_{a-b}(r) dr, \tag{2}$$

where r_{a-b} is the position of the minimum after the first peak of g_{a-b} . In this paper, we refer to N_a as the total coordination of species a (i.e., $N_a = \sum_b N_{a-b}$).

The atomic trajectories and asymptotic slope of the time-dependent mean-square displacement (MSD) in the simulation cells were used to check that cells are in the liquid state and to calculate the self-diffusion coefficient, D_a , for each species a following the Einstein relation (Allen and Tildesley 1991),

$$D_a = \lim_{t \rightarrow \infty} \frac{1}{N_a^*} \sum_{i=1}^{N_a^*} \frac{\langle (r_i(t + t_0) - r_i(t_0))^2 \rangle}{6t}, \tag{3}$$

where N_a^* is the total number of atoms of species a , $r_i(t)$ is the position of the i th atom at time t , and the angular brackets represent the ensemble average computed over different origin times (t_0) along the atomic trajectories. The Arrhenius relation was used to determine the effect of P and T according to

$$D = D_0 \exp\left(-\frac{Q}{RT}\right), \tag{4}$$

where D_0 is the pre-exponential diffusion coefficient, R is the universal gas constant, and Q the activation energy,

$$Q = \Delta H + P\Delta V. \tag{5}$$

ΔH and ΔV are the activation enthalpy and activation volume (i.e., P - and T -dependence terms), respectively, given as:

$$\frac{\partial \ln D}{\partial(1/T)} = -\frac{\Delta H}{R}, \tag{6}$$

$$\frac{\partial \ln D}{\partial P} = -\frac{\Delta V}{RT}. \tag{7}$$

Results and discussion

Structural properties and compression mechanisms

The partial radial distribution functions (RDFs) of pure liquid Fe and Ni and Fe–Ni alloys at the three volumes for the simulations at 3000 K are shown in Fig. 1, and those of Fe–C, Ni–C, and Fe–Ni–C in Fig. 2 for simulations with 4 at% C. Equivalent RDF plots of the Fe–C, Ni–C, and Fe–Ni–C simulations with 1 and 20 at% C, in addition to those at lower T , are provided in Figs. SM1–SM3 of the Supplemental Material. The radial position (r) and intensity (I) of the first RDF peaks are summarized for each atomic pair in Figs. 3 and 4, respectively, as a function of P , and the total coordination number of each species is shown in Fig. 5. The results indicate that atomic pairs can generally be classified into one of three categories: (1) Fe/Ni–Fe/Ni framework with $r = 2.18$ – 2.45 Å; (2) shorter scale Fe/Ni–C framework–quasi-interstitial interactions with $r = 1.83$ – 1.97 Å; and (3) short-scale C–C interstitial–interstitial interactions with $r = 1.29$ – 1.57 Å.

The compression behavior of liquids is dominated by a reduction of interatomic distances, increased coordination numbers, or a combination of the two. Although only three simulation volumes were investigated here owing to this study’s primary focus on compositional effects, important insight on the effect of P can be obtained by a careful inspection of the response of the liquid structural properties to isothermal compression. We therefore discuss the results in terms of the interatomic spacings (r), compression rates (dr/dP), intensities (I) of the first $g(r)$ peaks, and coordination changes (dN_a/dP), with r and N_a values listed in Table SM1.

Fe/Ni substitutional atoms

The average interatomic distances (r) between all substitutional atom pairs (i.e., $r_{\text{Fe-Fe}}$, $r_{\text{Fe-Ni}}$, $r_{\text{Ni-Ni}}$) generally decrease with P (Fig. 3a–c). The $r_{\text{Fe-Fe}}$ values are sensitive to both X_{Ni} and X_{C} , but the effects are opposite: $r_{\text{Fe-Fe}}$ decreases with X_{Ni} but increases with X_{C} (Fig. 3a). The compression rates ($dr_{\text{Fe-Fe}}/dP$) are considerably lower in the alloys (-1.51 ± 0.26 mÅ/GPa) than in pure liquid iron (labeled $r_{\text{Fe-Fe}^*}$ with $dr_{\text{Fe-Fe}^*}/dP = -2.25$ mÅ/GPa)

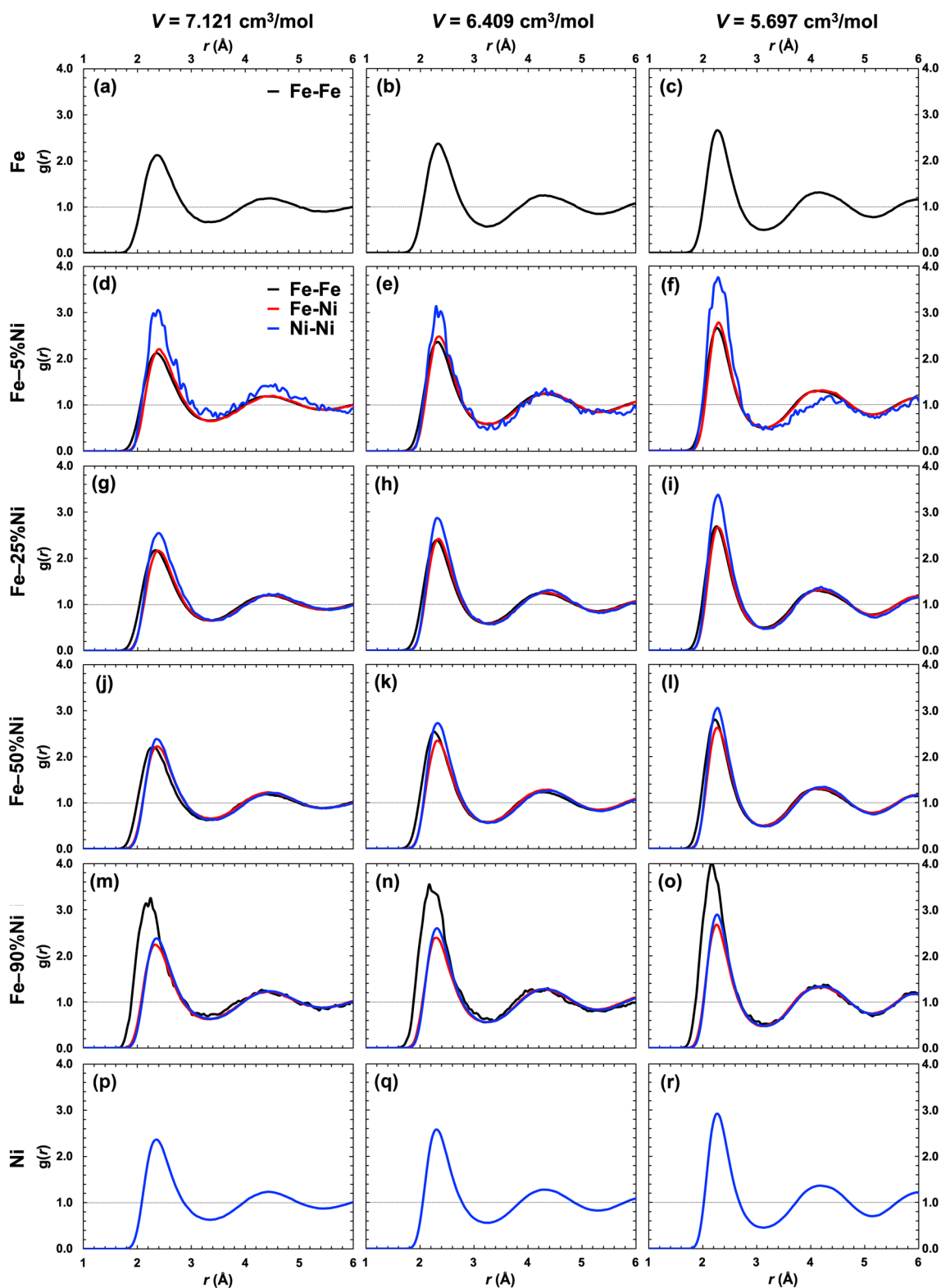


Fig. 1 Partial radial distribution functions (RDFs) for Fe–Ni alloys and end-member liquids at 3000 K for the large (7.121 cm³/mol; left column), intermediate (6.409 cm³/mol; middle column), and small (5.697 cm³/mol; right column) simulation cell volumes. The radial positions (r) of the first RDF peaks, which represent the average nearest neighbor distances between two atom pairs, decrease with P (i.e.,

cell volume), as summarized in Fig. 3. The radial positions of the first $r_{\text{Fe-Fe}}$ peaks gradually decrease with increasing X_{Ni} . The first RDF peak intensities (I) of all atomic pairs increase with P , as summarized in Fig. 4. $I_{\text{Fe-Fe}}$ and $I_{\text{Ni-Ni}}$ also increase with decreasing X_{Fe} and X_{Ni} , respectively, which implies stronger Fe–Fe and Ni–Ni ordering when present in dilute form

and decrease linearly with X_{Ni} ($R^2=0.72$). The $I_{\text{Fe-Fe}}$ values (Fig. 4a) are mostly insensitive to composition, with the notable exception of the highly Ni-rich simulations, for which binary Fe–90%Ni and ternary Fe–90%Ni–4%C show ~46% and ~21%–64% higher $I_{\text{Fe-Fe}}$ than $I_{\text{Fe-Fe}^*}$, respectively, and the differences in the latter composition increase with P . This demonstrates that Fe–Fe pairs are highly ordered—and closer to one another, as mentioned above—when present in a relatively dilute concentration.

Average $r_{\text{Ni-Ni}}$ values in pure liquid Ni (hereafter $r_{\text{Ni-Ni}^*}$) are approximately 2% (~0.05 Å) longer than $r_{\text{Fe-Fe}^*}$ with a slightly higher compression rate ($dr_{\text{Ni-Ni}^*}/dP = -2.35 \text{ mÅ/GPa}$) (Fig. 3b). The addition of Ni therefore slightly modifies the structure of the metallic liquid and average quasi-interstitial void volumes, in contrast to Si, which directly substitutes for Fe in binary and ternary liquid alloys (e.g., Pozzo et al. 2013; Posner et al. 2017b; Posner and Steinle-Neumann 2019) with essentially zero size mismatch (i.e., $r_{\text{Fe-Si}} = r_{\text{Fe-Fe}} = r_{\text{Fe-Fe}^*}$). The $I_{\text{Ni-Ni}}$ values are consistently higher than those of $I_{\text{Fe-Fe}^*}$ (Fig. 4b) and generally decrease with X_{Ni} . Some low-Ni ($X_{\text{Ni}} \leq 0.05$) compositions show exceptionally high $I_{\text{Ni-Ni}}$ values, similar to the very high $I_{\text{Fe-Fe}}$ values in low-Fe compositions (Fig. 4a), which demonstrates that Ni–Ni pairs are also somewhat more correlated when present in dilute form. On the other hand, some of the $g_{\text{Ni-Ni}}(r)$ curves for compositions with $X_{\text{Ni}} \leq 0.02$ do not present a well-defined Ni–Ni peak within the typical range for substitutional pairs (e.g., 2.1–2.5 Å) and are therefore excluded from the summary plots in Figs. 3b and 4b.

Average $r_{\text{Fe-Ni}}$ (Fig. 3c) are generally slightly larger (up to ~5%) than $r_{\text{Fe-Fe}^*}$ and $r_{\text{Fe-Fe}}$ in the respective compositions, which is similar with the results of our previous computational study involving Fe–4%Ni over a wider T range (Posner and Steinle-Neumann 2019), with the exception of Fe–90%Ni, for which $r_{\text{Fe-Ni}} < r_{\text{Fe-Fe}^*}$. Similar to the $r_{\text{Fe-Fe}}$ results, $r_{\text{Fe-Ni}}$ values are also found to be sensitive to composition: $r_{\text{Fe-Ni}}$ decreases with X_{Ni} and increases with X_{C} , which further demonstrates that Ni and C alloy components impose opposite structural effects on liquid Fe. The $I_{\text{Fe-Ni}}$ values generally decrease with X_{Ni} and scatter both above and below the $I_{\text{Fe-Fe}^*}$ curve (Fig. 4c).

The coordination numbers of Fe (Fig. 5a) and Ni (Fig. 5b) range between ~11.6 and ~13.7, which indicates that both species are essentially close-packed over the full investigated P range. The coordination numbers of Fe and Ni in the pure end-member liquids generally define the upper limits of both, and compositions with $X_{\text{Ni}}=0.9$ yield slightly lower N_{Fe} than the others.

Relation between Fe/Ni substitutional and C quasi-interstitial atoms

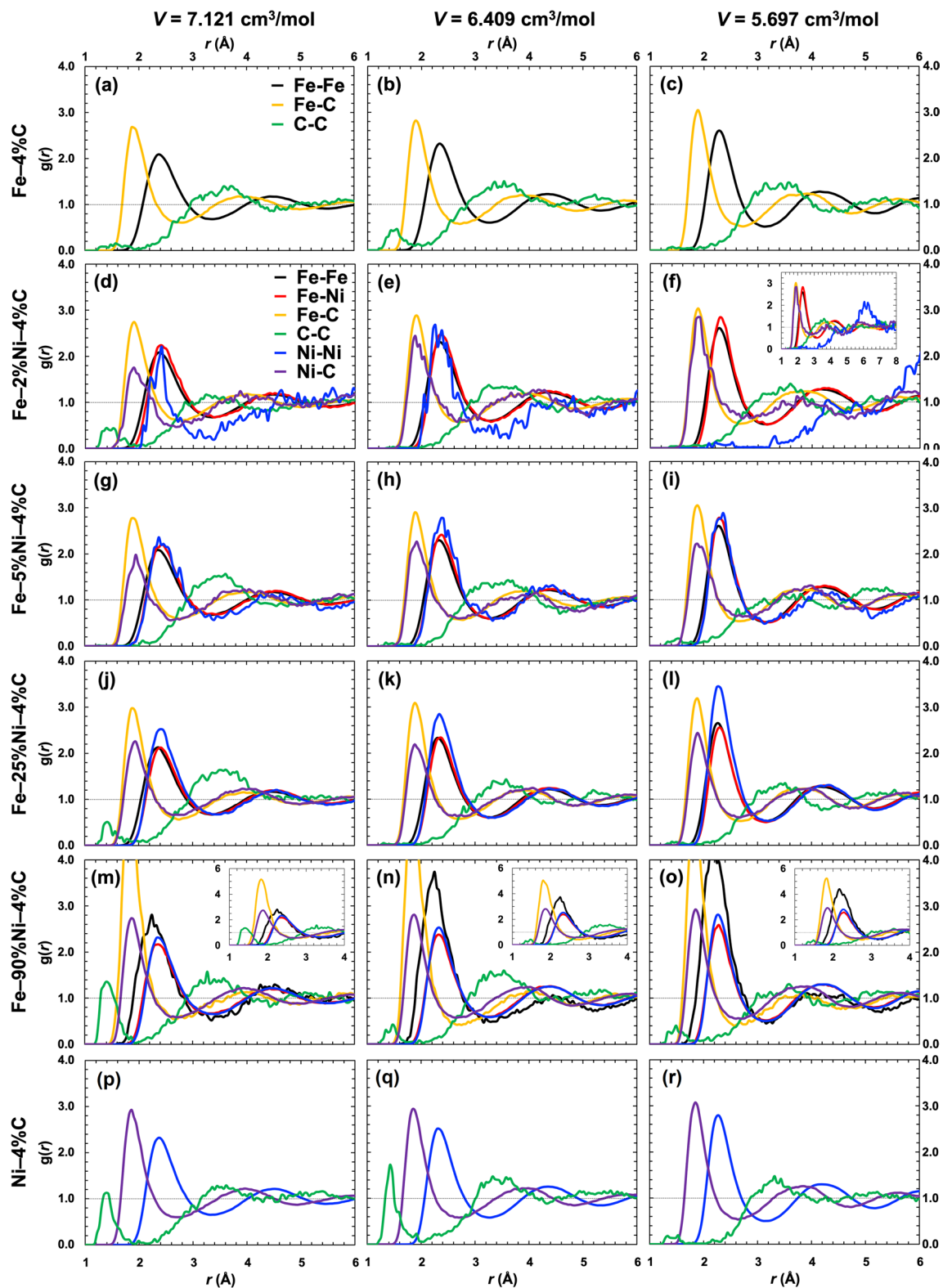
Average $r_{\text{Fe-C}}$ (Fig. 3d) and $r_{\text{Ni-C}}$ (Fig. 3e) are both approximately 16%–22% shorter than $r_{\text{Fe-Fe}}$ and $r_{\text{Ni-Ni}}$, respectively; these differences decrease with P , which is

similar to previous results for liquid Fe–4%C, Fe–4%O, and Fe–4%N by Posner and Steinle-Neumann (2019). Both $r_{\text{Fe-C}}$ and $r_{\text{Ni-C}}$ values are sensitive to Ni content, decreasing essentially linearly with X_{Ni} by up to 4% for $X_{\text{Ni}}=0.9$ compared with values for $X_{\text{Ni}} \leq 0.02$. This is also demonstrated in a comparison of Fig. 3d and e, which shows that Ni-free Fe–C compositions have the largest $r_{\text{Fe-C}}$ and Fe-free Ni–C compositions have the smallest $r_{\text{Ni-C}}$. In contrast with the $r_{\text{Fe-Fe}}$ and $r_{\text{Fe-Ni}}$ results presented in the previous section, X_{C} has a negligible influence on $r_{\text{Fe-C}}$ and $r_{\text{Ni-C}}$.

The $r_{\text{Fe-C}}$ and $r_{\text{Ni-C}}$ compression trends also differ from those of the Fe/Ni atomic pairs. In nearly all compositions, $r_{\text{Fe-C}}$ values (Fig. 3d) remain constant over the two lowest- P simulations (i.e., $dr_{\text{Fe-C}}/dP=0$), which is accompanied by a coordination increase of ~6.8 to ~8.0 (Fig. 5c), and then decrease with increasing P at a rate of approximately $dr_{\text{Fe-C}}/dP = -0.5 \text{ mÅ/GPa}$ (Fig. 3d) with a continuing increase in coordination number to ~8.6. A similar observation was previously reported for oxygen in liquid Fe–O over a larger P range (e.g., Ichikawa and Tsuchiya 2015; Posner et al. 2017c), with similar structural properties to carbon in liquid iron alloys (i.e., $r_{\text{Fe-C}} \sim r_{\text{Fe-O}}$, $N_{\text{C}} \sim N_{\text{O}}$; Posner and Steinle-Neumann 2019): $r_{\text{Fe-O}}$ remained essentially constant with increasing P while N_{O} increased to ~8, then decreased monotonically upon a further P increase to ~300 GPa, over which range N_{O} stayed essentially fixed and did not exceed ~9.

Figure 4d shows that $I_{\text{Fe-C}}$ values strongly depend on X_{Ni} , ranging from ~2.8–3.3 for Ni-poor compositions to 3.8–4.0 for $X_{\text{Ni}}=0.5$ and as high as 5.0–5.2 for $X_{\text{Ni}}=0.9$. This indicates that Fe–C pairs become increasingly ordered (and shorter) with decreasing Fe concentration, which is consistent with the Fe–Fe results presented in the previous section. The $I_{\text{Ni-C}}$ values in Fig. 4e are consistently lower than $I_{\text{Fe-C}}$ and insensitive to composition.

The $r_{\text{Ni-C}}$ values are shown in Fig. 3e as a function of P alongside the $r_{\text{Fe-C}}$ trend line of Fe–4%C for comparison. Especially at low P , the range of $r_{\text{Ni-C}}$ values is wide and shows a clear decrease of $r_{\text{Ni-C}}$ with increasing X_{Ni} , ranging 1.93–1.97 Å for simulations with $X_{\text{Ni}}=0.01$ –0.02 to 1.86–1.87 Å for simulations with $X_{\text{Ni}} > 0.9$. The results generally show that $r_{\text{Ni-C}} > r_{\text{Fe-C, Fe-4%C}}$ for $X_{\text{Ni}} < 0.5$ and $r_{\text{Ni-C}} < r_{\text{Fe-C, Fe-4%C}}$ for $X_{\text{Ni}} > 0.5$. The $r_{\text{Ni-C}}$ compression trend is less straightforward than that of $dr_{\text{Fe-C}}/dP$: approximately half of the studied compositions show the same behavior as $dr_{\text{Fe-C}}/dP$ (i.e., no change in r between the lowest two P points, followed by a decrease upon further increasing P), whereas most of the others decrease continuously with P . There is no systematic trend related to composition to explain this difference; both patterns occur in compositions with high and low Ni and C contents. In contrast, 11 of 15 compositions show a “plateau-decrease”



trend of $r_{\text{Fe-C}}$ with P . This difference might be explained by preferential packing of Fe around C.

Carbon quasi-interstitial clustering

As also reported in a previous study on binary liquid Fe-C (Ohmura et al. 2020), most compositions show short-range

Fig. 2 Partial radial distribution functions (RDFs) for (a–c) Fe–4% C, (d–o) Fe–Ni–4% C, and (p–r) Ni–4% C liquid alloys at 3000 K at the same simulation cell volumes as in Fig. 1. Short-range C–C peaks (green curves, referred to as C–C′) indicate tight carbon clustering in most cells, with peak intensities (*I*) greater than 1 in some Ni-rich compositions (m, p, q), whereas most other compositions show more broad, low-*I*_{C–C′} peaks, as shown in Fig. 4f as a function of *P* and Fig. SM4 as a function of *X*_{Ni}. The *r*_{Fe–C} and *r*_{Ni–C} values are approximately 16%–22% shorter than *r*_{Fe–Fe} in the respective compositions, and the difference generally increases with *P*. The positions of the first *g*_{Fe–Fe}(*r*) and *g*_{Fe–C}(*r*) peaks in the most Ni-rich ternary alloy (Fe–90%Ni–4% C) (m–o), respectively, occur at 2%–5% and 2%–3% shorter *r* than in the other Fe–C and Fe–Ni–C alloys, as summarized in Fig. 3. The *I*_{Fe–C} values are consistently higher than those of *I*_{Ni–C}, as summarized in Fig. 4

C–C clustering (Fig. 2) with peak positions (referred to as *r*_{C–C′}) on the order of ~1.29–1.57 Å, which is within the range of *r*_{C–C} in graphite (1.42 Å) and diamond (1.54 Å) (e.g., Harrison 1980). Differing from the *dr/dP* behavior of the Fe/Ni–Fe/Ni and Fe/Ni–C pairs, most *r*_{C–C′} values are observed to continuously increase with *P*, with the exception of Fe–4% C, for which *r*_{C–C′} decreases with *P*, and some carbon-rich (*X*_C=0.2) compositions where *r*_{C–C′} values remain largely unchanged over the full *P* range.

It is important to note that when present, most C–C′ peaks exhibit low *g*(*r*) intensities (*I* < 1; Fig. 4f), whereas others—particularly in the Fe-poor or Fe-free compositions—exhibit *I* > 1, reaching as high as ~2.1 in liquid Ni–20% C at low *P*, as summarized in Fig. SM4. We interpret the general increase of *I*_{C–C′} with *X*_{Ni} to result from Ni–C repulsion that likely reduces the stability (i.e., solubility) of carbon in the liquid. The quantification of chemical potentials in the liquid (e.g., using techniques such as thermodynamic integration) is required to better resolve this question.

The overall positive *dr*_{C–C′}/*dP* trend correlates with generally decreasing *I*_{C–C′} values with *P* (i.e., *dI*_{C–C′}/*dP* < 0; Fig. 4f), which is opposite to the behavior for the Fe/Ni–Fe/Ni and Fe/Ni–C pairs, where *dI*/*dP* > 0. These structural features are related to the gradually increasing occupation of carbon atoms from ~6.2 to 7.4 at low *P* (representing quasi-octahedral voids in the quasi close-packed metal framework) to ~8.1–8.6 at high *P* (representing an approximate B2 packing structure). The occurrence and intensity of carbon clustering generally decreases once the coordination change is completed.

Repulsion forces and preferential coordination environments

If Fe and Ni are assumed to be essentially equivalent species (i.e., “geochemical twins”) in liquid Fe–Ni and Fe–Ni–C alloys, their proportional contribution to a given total coordination number should be equal to their atomic fraction. If

true, the following deviation *f* (in %) would be expected to be approximately zero,

$$f = \frac{A - C}{C} \times 100, \tag{8}$$

with

$$A = \frac{N_{a-Fe}}{N_{a-Fe} + N_{a-Ni}}, \tag{9}$$

and

$$C = \frac{X_{Fe}}{X_{Fe} + X_{Ni}}. \tag{10}$$

We tested this hypothesis and found that it generally does not hold in liquid Fe–Ni and Fe–Ni–C, especially for compositions with *X*_{Ni} > 0.25 (Fig. 6). The results for carbon were most striking, showing a very strong tendency to coordinate with Fe over Ni, with a strong increase of *f* with Ni content. This can be rationalized by the metal–carbon phase relations: while Fe₃C is stable at ambient *P* as a eutectic phase (Wood 1993) and Fe₇C₃ forms at high *P* (Nakajima et al. 2009), Ni₃C has only recently been synthesized at much higher *P* (Fedotenko et al. 2021). More surprisingly, the *f* values for Fe and Ni differ from zero and the difference grows with *X*_{Ni}, increasing for Fe and decreasing for Ni. This implies that Fe and Ni more strongly concentrate around themselves than around each other, and a direct comparison of coordination ratios, (*N*_{Fe–Fe}/[*N*_{Fe–Fe} + *N*_{Fe–Ni}]) > *X*_{Fe}, (*N*_{Ni–Ni}/[*N*_{Ni–Ni} + *N*_{Ni–Fe}]) > *X*_{Ni}, (*N*_{Ni–Fe}/[*N*_{Ni–Ni} + *N*_{Ni–Fe}]) < *X*_{Fe} and (*N*_{Fe–Ni}/[*N*_{Fe–Fe} + *N*_{Fe–Ni}]) < *X*_{Ni}, confirms this observation, including for the binary Fe–Ni. This implies non-ideal mixing of Fe and Ni both in the C-free and C-bearing compositions, a result that is consistent with the observation of an excess volume of mixing in the Fe–Ni binary liquid at ambient *P* (Watanabe et al. 2016). Combined, these two observations negate the assumption that Fe and Ni are “geochemical twins”.

Transport properties

Beyond an equilibration time of < 1 ps, the slopes of the MSD curves for all simulations (Figs. SM5 and SM6), as well as those at the lowest *T* (1675 K) considered for a comparison with the results of Wang et al. (2019), show quasi-linear behavior, which indicates that these are in the liquid state and that the MSD can be used reliably to determine a diffusion constant based on the Einstein relation (Eq. (4)). However, MD simulations with the number of atoms we use here are well known to require significant undercooling before a solid forms from the liquid (e.g., Luo et al. 2003; Braithwaite and Stixrude 2019).

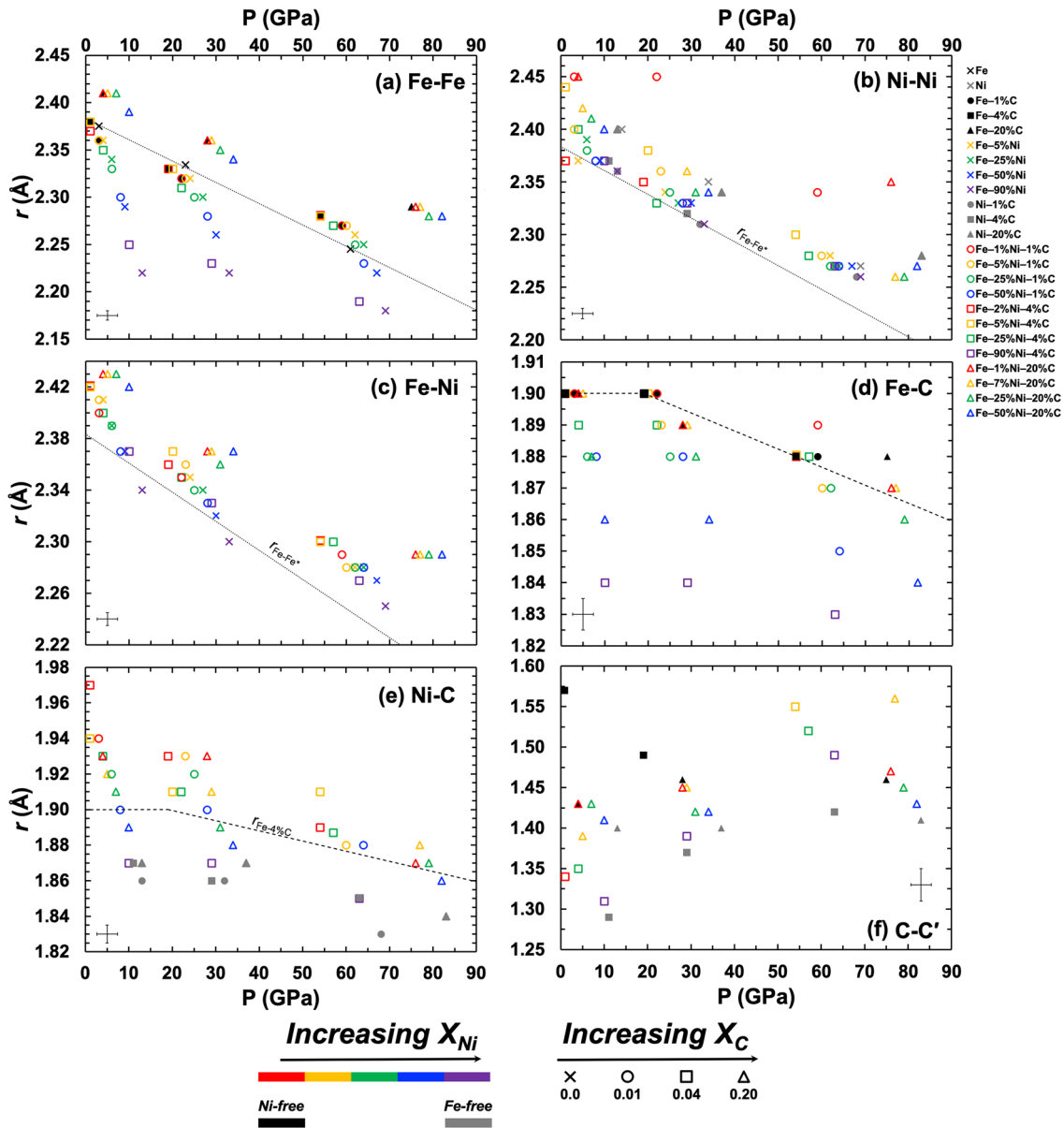


Fig. 3 Average radial positions (i.e., interatomic distances) of the first $g(r)$ peaks for all investigated compositions as a function of P . The symbol color represents nickel content (X_{Ni}) and follows a basic rainbow scheme with increasing X_{Ni} : red, orange, green, blue, and purple symbols represent $X_{\text{Ni}} = \sim 0.01, \sim 0.05, 0.25, 0.5,$ and 0.9 , respectively. The symbol shape represents carbon content (X_C): crosses, circles, squares, and triangles represent $X_C = 0, 0.01, 0.04,$ and 0.2 , respectively. The symbol filling distinguishes if Fe AND Ni are included in the liquid composition (unfilled) versus if Fe OR Ni are present (filled). The dotted trend lines in **a–c** show the linear fit to $r_{\text{Fe-Fe}}$ in pure Fe (referred to as $r_{\text{Fe-Fe}^*}$), and the dashed trend lines in **(d)** and **(e)** show the step-wise fit to $r_{\text{Fe-C}}$ for Fe-4% C. Average 2σ error bars are shown in the lower corners of each panel. The results show that **(a–c)** $r_{\text{Fe-Fe}}, r_{\text{Fe-Ni}},$ and $r_{\text{Ni-Ni}}$ generally decrease with P , whereas **(d,**

e) $r_{\text{Fe-C}}$ and $r_{\text{Ni-C}}$ values, which are 16%–22% shorter than $r_{\text{Fe-Fe}}$ and $r_{\text{Ni-Ni}}$, respectively, remain mostly constant between the two lowest P points, coinciding with a coordination change from ~ 6.8 to ~ 8.0 (Fig. 5), and then decrease upon further P increase once the coordination change is complete. In contrast, the $r_{\text{C-C}'}$ values in **(f)**, which represent the position of the short-range carbon clustering peak (i.e., not the broad second peak near ~ 3.5 Å), generally increase with P , which reflects the larger average void size for the higher coordination carbon. The average distances between all atomic pairs except for C–C' generally decrease with X_{Ni} , particularly for $r_{\text{Fe-Fe}}, r_{\text{Fe-C}},$ and $r_{\text{Ni-C}}$. The $r_{\text{Fe-Fe}}$ and $r_{\text{Fe-Ni}}$ values also increase with X_C . Some Ni-poor compositions show no Ni–Ni peak or only very large- r peaks (~ 6.2 Å; Fig. 1f, inset) and are therefore not included here

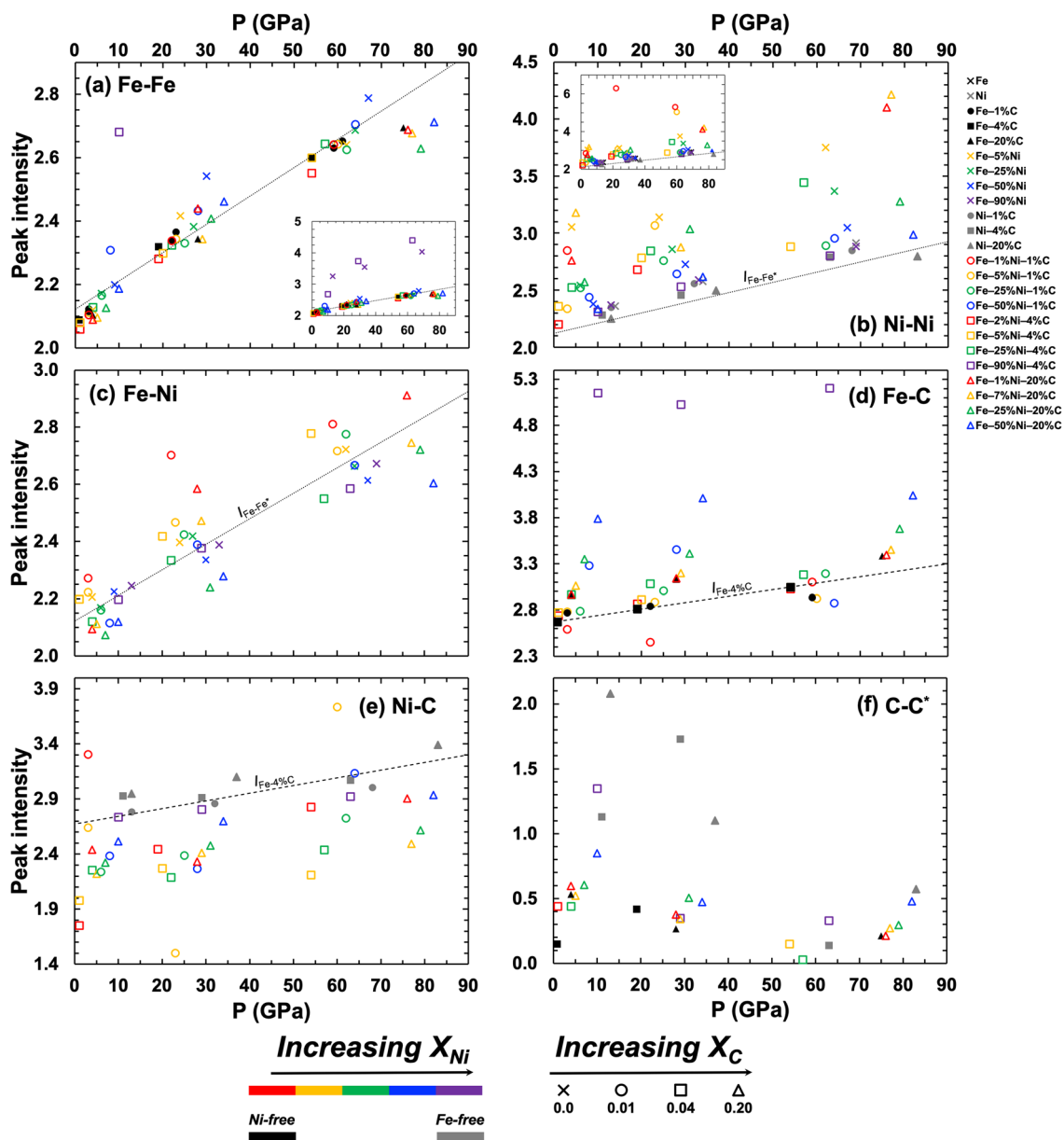


Fig. 4 Intensities of the first $g(r)$ peaks (I), which generally reflect the degree of chemical ordering. The dotted trend lines in (a–c) show the linear fit to I_{Fe-Fe} values in pure liquid Fe (i.e., I_{Fe-Fe^*}). The dashed trend lines in (d) and (e) show a linear fit to I_{Fe-C} values in liquid Fe-4% C. (a) For most compositions, I_{Fe-Fe} are similar and increase at a similar rate with P , with the notable exceptions of the alloys with $X_{Ni}=0.9$, which show ~21%–64% higher I_{Fe-Fe} than I_{Fe-Fe^*} (inset) and the difference generally increases with P . (b) I_{Ni-Ni} are generally greater than I_{Fe-Fe^*} and increase with decreasing X_{Ni} , whereas (c) I_{Fe-Ni} vary both above and below I_{Fe-Fe^*} . Some Ni-poor ($X_{Ni} \leq 0.05$)

simulations show exceptionally high I_{Ni-Ni} values, similar to the very high I_{Fe-Fe} values in the Fe-poor compositions in (a). As in Fig. 3b, I_{Ni-Ni} values are not shown for Ni-poor simulations with peaks occurring at very large r (e.g., Fig. 2f, inset). (d) I_{Fe-C} values increase with X_{Ni} , which implies higher Fe–C ordering with decreasing Fe concentration. In contrast, (e) I_{Ni-C} are generally insensitive to composition and lower than I_{Fe-C} . (f) I_{C-C^*} values of the short-range $g_{C-C^*}(r)$ peak are mostly very low, except for the Ni-rich compositions, and generally decrease with P and increase with X_{Ni} (Fig. SM4)

Effect of pressure

The self-diffusion coefficients of Fe, Ni, and C at 3000 K in all compositions are shown as a function of P in Fig. 7a–c, respectively, and listed in Table SM2. The dotted lines

shown in Fig. 7a, b indicate the linear trend of D_{Fe} with P in pure liquid. The results indicate that D_{Fe} values are generally equal to D_{Ni} and approximately 2–3 times slower than D_C for all investigated alloy compositions, which agrees with previous studies of both binary Fe–Ni and Fe–C (Posner

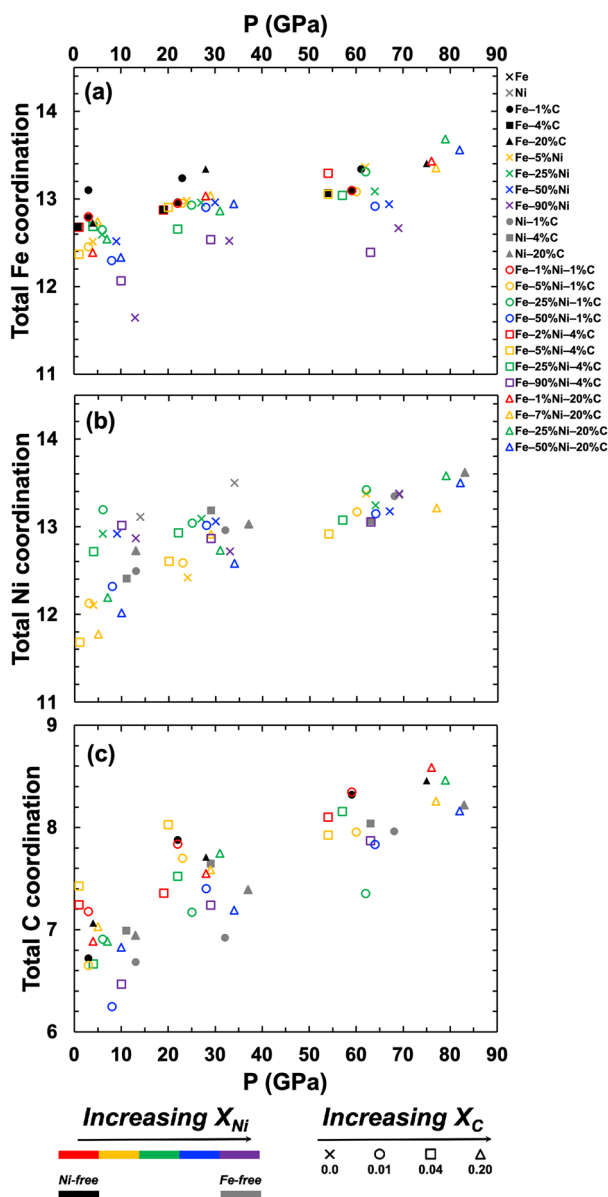


Fig. 5 Total coordination numbers for (a) Fe, (b) Ni, and (c) C. Fe and Ni are both generally close packed over the full range of study, whereas C coordination increases from ~ 6.2 – 7.4 (quasi-octahedral) to ~ 8.1 – 8.6 (B2 packing) with increasing P . Fe-rich compositions tend to show slightly higher N_{Fe} than Fe-poor compositions, whereas a compositional trend is less notable for N_{Ni} and N_{C} , although N_{Ni} in pure liquid Ni is generally higher than N_{Ni} in most other compositions

and Steinle-Neumann 2019) and ternary Fe–Ni–C liquids conducted over a considerably smaller compositional range (Wang et al. 2019).

The pressure dependence (ΔV) at 3000 K was determined using a least-squares best fitting to Eq. (4), yielding 0.52 ± 0.06 , 0.53 ± 0.08 , and 0.46 ± 0.10 cm^3/mol for Fe, Ni, and C, respectively, which is consistent with previous experiments and computations on Fe–Si, Fe–O, and

Fe–Cr liquid compositions (Posner et al. 2017a–c). The highest obtained ΔV value was 0.77 ± 0.06 cm^3/mol for Ni diffusion in pure liquid Ni; the lowest obtained ΔV value was 0.24 ± 0.06 cm^3/mol for C diffusion in liquid Ni–4% C (Table SM2).

Figure 7c compares our D_{C} results with the diffusion data from high- P experiments involving binary Fe–C liquid alloys by Rebaza et al. (2021) and Dobson and Wiedenbeck (2002) extrapolated to 3000 K and the relevant P range (labeled dashed lines). The extrapolation curve of Rebaza et al. (2021) is comparable with the low- P D_{C} values for liquid Fe–C (filled black symbols) obtained here, but the mismatch increases with P owing to their very small reported ΔV . Dobson and Wiedenbeck (2002) reported a much larger activation volume and their extrapolation curve is substantially above and below the D_{C} obtained here at low- and high- P , respectively, with an overlap limited to values at approximately 30 GPa. Our findings indicate that an intermediate value between the two studies of $\Delta V \sim 0.5$ cm^3/mol best represents the diffusion of Fe, Ni, and C over the investigated P – T range.

Effect of temperature

The T dependence of diffusion was determined for Fe–7%Ni–20%C, which was also chosen for direct comparison with the results by Wang et al. (2019) at 1675 K and $P \geq 5$ GPa. To complement our 3000-K results for this composition, we performed five additional simulations: two at 1675 K using cell volumes of $V_{0.8}$ (16 ± 2 GPa) and $V_{0.7}$ (61 ± 2 GPa), and three at 2350 K using cell volumes of $V_{0.9}$ (0.1 ± 2 GPa), $V_{0.8}$ (23 ± 2 GPa), and $V_{0.7}$ (69 ± 3 GPa). Our 1675-K diffusion results (Fig. 8) are in good agreement with those of Wang et al. (2019) despite the different treatment on spin-polarization, with ΔV values of 0.65, 0.75, and 0.61 cm^3/mol for Fe, Ni, and C, respectively. Wang et al. (2019) performed a detailed isothermal study (1675 K) on liquid Fe–7%Ni–20%C at P up to 67 GPa and reported a substantial reduction of the ΔV of Fe/Ni and C diffusion at ~ 5 GPa, from 1.4 ± 0.3 and 1.2 ± 0.3 cm^3/mol for $P < 5$ GPa to 0.77 ± 0.06 and 0.61 ± 0.09 cm^3/mol for $P > 5$ GPa, respectively, the latter of which are consistent with our values. This change in diffusivity may be related to the onset of the loss of magnetic moments in the spin-polarized simulations of Wang et al. (2019), which can explain why we recover their diffusivities in the non-magnetic simulations, although Wang et al. (2019) report magnetic moments to persist throughout the compression range they consider. With the rapid decrease of effective magnetic moments with T shown in a DFT-MD study on liquid Fe (Korell et al. 2019), we do not expect that magnetism would influence the diffusion results at 2350 and 3000 K. The ΔV values at 2350 K of 0.54 ± 0.03 , 0.54 ± 0.11 , and 0.50 ± 0.01 cm^3/mol for Fe, Ni,

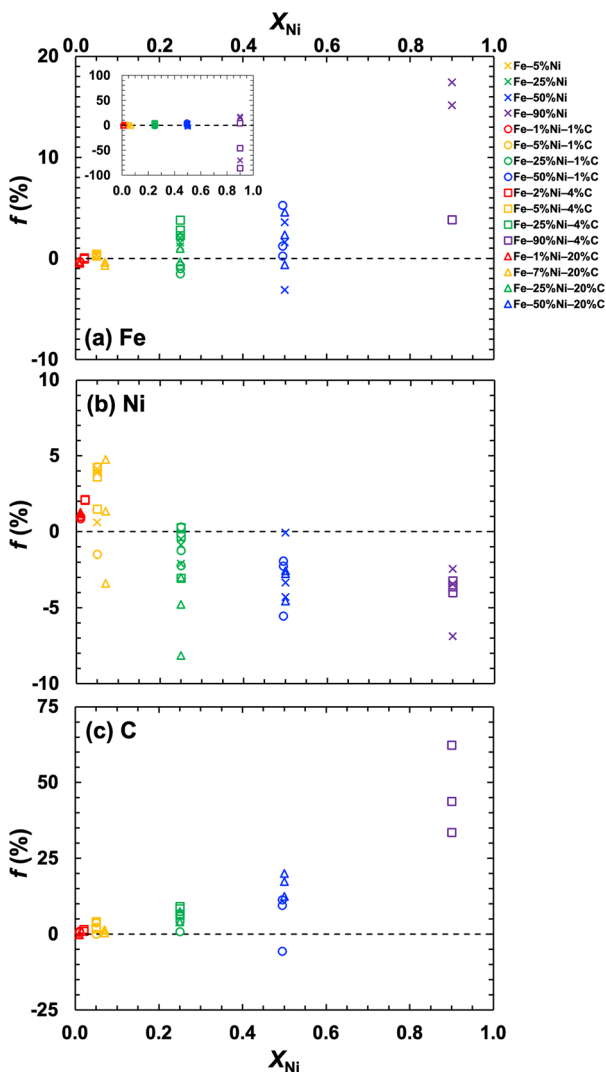


Fig. 6 Percent deviation f of the proportion of Fe atoms contributing to the total number of framework atoms (Fe+Ni) comprising the average coordination number of (a) Fe, (b) Ni, and (c) C, as defined in Eqs. (8)–(10). Dashed vertical lines indicate zero deviation, for which Fe and Ni are essentially identical substitutional species. Despite some scatter in (a) for high X_{Ni} , the results show that Fe atoms generally tend to preferentially coordinate with other Fe atoms and C atoms compared with Ni atoms, i.e., positive deviations in (a) and (c), and less preferentially around Ni atoms, i.e., negative deviations in (b)

and C, respectively, are more consistent with the results at 3000 K (Table SM2). A slight reduction of ΔV (i.e., $\partial D/\partial P$) with T implies that the differences of D values between the metal atoms and carbon at 1675 and 3000 K increase with P , e.g., from ~ 0.7 log unit at 5 GPa to ~ 1.5 log units at 67 GPa.

Combining our results with those of Wang et al. (2019) to fit Eq. (4) yields $D_0 = (1.00 \pm 0.08) \times 10^{-7} \text{ m}^2/\text{s}$, $\Delta H = 56 \pm 2 \text{ kJ/mol}$, and $\Delta V = 0.49 \pm 0.02 \text{ cm}^3/\text{mol}$ for Fe/Ni and $D_0 = (1.4 \pm 0.1) \times 10^{-7} \text{ m}^2/\text{s}$, $\Delta H = 50 \pm 2 \text{ kJ/mol}$, and $\Delta V = 0.47 \pm 0.02 \text{ cm}^3/\text{mol}$ for C. The results of this global

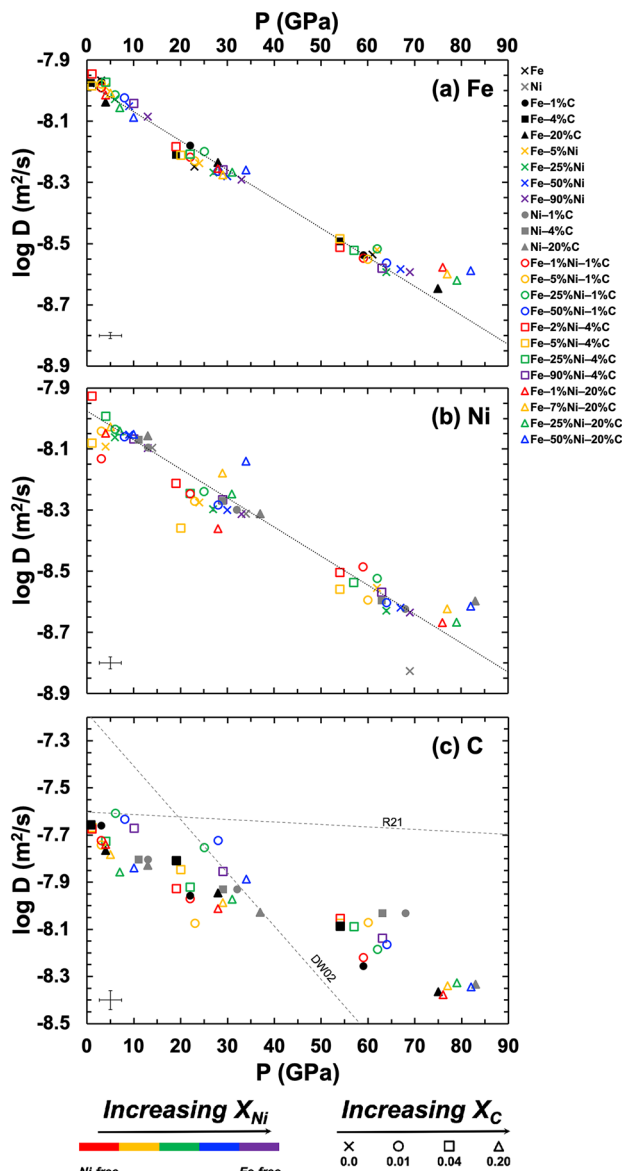


Fig. 7 Self-diffusion coefficients D of (a) Fe, (b) Ni, and (c) C for the investigated compositions at 3000 K. The dotted lines in (a) and (b) show the linear fit to D_{Fe} in pure liquid Fe. The dashed lines in (c) show curves extrapolated using the Arrhenian diffusion parameters reported from high- P experiments in liquid Fe–C by Dobson and Wiedenbeck (2002) (DW02) and Rebaza et al. (2021) (R21). The simulation results yield activation volumes mostly on the order of $0.4\text{--}0.6 \text{ cm}^3/\text{mol}$ for all species, which is consistent with previous DFT-MD studies and falls in between the experimental values reported by Dobson and Wiedenbeck (2002) and Rebaza et al. (2021). Average 2σ error bars are shown in the left corners of each panel

fit are shown as dashed curves in Fig. 8 alongside dotted curves for the fits to each isotherm. The fitting results provide a good match with the diffusion coefficients at 2350 and 3000 K, but the P -slope of the global model at 1675 K is approximately a factor of two less steep than the isothermal

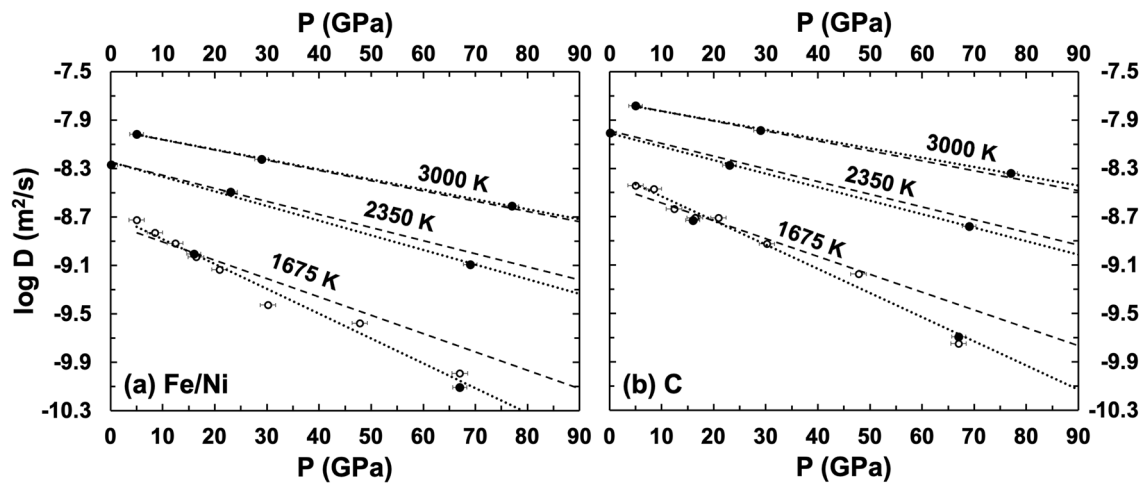


Fig. 8 Self-diffusion coefficients D of (a) Fe/Ni and (b) C in liquid Fe–7%Ni–20%C at 1675, 2350, and 3000 K. Values reported by Wang et al. (2019) at 1675 K and ≥ 5 GPa are shown as open symbols and those obtained here are shown as filled symbols. The dashed curves show the global model fit (including points at all three T) according to Eq. (4) and the dotted curves show the individual

P trends obtained at each isotherm. The activation volumes (i.e., slope of $\log D$ versus P) at 2350 and 3000 K are generally similar ($\Delta V_{\text{Fe/Ni}} \sim 0.51$ cm³/mol, $\Delta V_{\text{C}} \sim 0.47$ cm³/mol) and the global model fit well reflects the P trend of the results, whereas those at 1675 K are slightly larger ($\Delta V_{\text{Fe/Ni}} \sim 0.70$ cm³/mol, $\Delta V_{\text{C}} \sim 0.61$ cm³/mol) and thus slightly mismatch with the global fit

fit for both Fe/Ni and C. A possible explanation for this discrepancy is that the 1675-K runs may actually involve a metastable liquid, as discussed above. The low- T results should therefore be applied with caution. Nevertheless, the model fits to Eq. (4) are comparable regardless of whether the 1675-K results are in- or excluded.

The obtained magnitudes of ΔH and ΔV are consistent with those previously reported for self-diffusion in binary Fe–Si and Fe–Cr liquids (Posner et al. 2017b). Therefore, these parameters are expected to be good approximations for the full range of pure, binary, and ternary liquids investigated here owing to the negligible effect of composition on D , although the effect of T was only tested for one composition.

Negligible effect of composition

The diffusive transport properties are found to be insensitive to composition over the P – T – X range of study, which does not support the hypothesis proposed by Rebaza et al. (2021) that the addition of Ni to liquid Fe–C affects carbon diffusivity. This discrepancy can be rationalized by two main factors: (1) The negligible pressure effect on D_{C} reported by the experiments by Rebaza et al. (2021) is not reproduced here or elsewhere (e.g., Dobson and Wiedenbeck 2002; Wang et al. 2019), which implies that the extrapolation of D_{C} using the parameters reported in Rebaza et al. (2021) to higher P than their experimental range (> 15 GPa) most likely result in an overestimate; (2) as mentioned in the previous section, the relatively low D values reported by Wang et al. (2019) are well reproduced here and may reflect liquid metastability

at 1675 K, further increasing the disparity between their results with those of Rebaza et al. (2021). Nevertheless, the question of coupled compositional effects on transport properties in ternary or higher order systems will be interesting to test with respect to planetary core analogs, particularly if they contain sulfur or hydrogen.

Conclusions

Nickel has been excluded from all previous high- P diffusion experiments involving liquid iron alloys, as well as the majority of computational studies. The results presented here indicate that Ni and C additions to liquid Fe affect the liquid alloy structural properties. One might intuitively expect that higher concentrations of slightly larger Ni atoms (or smaller C atoms) would gently expand (contract) the Fe framework, i.e., increase (reduce) $r_{\text{Fe-Fe}}$; however, the opposite is observed: $r_{\text{Fe-Fe}}$ decreases (increases) with increasing X_{Ni} (X_{C}). Fe and Ni also show preferential packing behaviors: they each prefer to pack around themselves than each other, and Fe more strongly coordinates around C than Ni. The effect of composition on the transport properties of the investigated alloys is essentially negligible, by contrast. The combined effect of Ni and other LEs (e.g., S, O, Si, H, N) on the structural and transport properties of multi-component liquid Fe alloys should be explored in the future, both computationally and in the laboratory, to more systematically understand the influence of alloy composition on the

metal-silicate partitioning behavior of relevant LEs during core formation.

Supplementary Information The online version contains supplementary material available at <https://doi.org/10.1007/s00269-022-01219-0>.

Acknowledgements We thank L. Yuan for his assistance in software design. Comments by the associate editor and two reviewers significantly improved the manuscript. All results are provided in the supporting information. Funding for this project was provided by the Deutsche Forschungsgemeinschaft with grant no. STE1105/13-2 in the Research Unit FOR2440. Computations were performed at the Leibniz Supercomputing Center of the Bavarian Academy of Sciences and Humanities.

Authors' contributions ESP designed the project, performed simulations, and wrote the manuscript. GSN supervised the project, performed simulations, and edited the manuscript.

Funding Open Access funding enabled and organized by Projekt DEAL. Funding for this project was provided by the Deutsche Forschungsgemeinschaft with grant no. STE1105/13-2 in the Research Unit FOR2440.

Declarations

Competing interests The authors declare no competing interests.

Conflict of interest The authors declare that they have no conflict of interest.

Open Access This article is licensed under a Creative Commons Attribution 4.0 International License, which permits use, sharing, adaptation, distribution and reproduction in any medium or format, as long as you give appropriate credit to the original author(s) and the source, provide a link to the Creative Commons licence, and indicate if changes were made. The images or other third party material in this article are included in the article's Creative Commons licence, unless indicated otherwise in a credit line to the material. If material is not included in the article's Creative Commons licence and your intended use is not permitted by statutory regulation or exceeds the permitted use, you will need to obtain permission directly from the copyright holder. To view a copy of this licence, visit <http://creativecommons.org/licenses/by/4.0/>.

References

- Allen MP, Tildesley DJ (1991) Computer simulation of liquids. Clarendon Press, Oxford
- Anderson HC (1980) Molecular dynamic simulations at constant pressure and/or temperature. *J Chem Phys* 72(4):2384–2393
- Benedix GK, Haack H, McCoy TJ (2014) Iron and stony-iron meteorites. In: Holland HD, Turekian KK (eds) Treatise on geochemistry 1, 267–285
- Braithwaite J, Stixrude L (2019) Melting of CaSiO₃ perovskite at high pressure. *Geophys Res Lett* 46:2037–2044
- Capobianco CJ, Drake MH, de'Aro, J. (1999) Siderophile geochemistry of Ga, Ge, and Sn: Cationic oxidation states in silicate melts and the effect of composition in iron–nickel alloys. *Geochim Cosmochim Acta* 17:2667–2677
- Corgne A, Keshav S, Wood BJ, McDonough WF, Fei Y (2008) Metal-silicate partitioning and constraints on core composition and oxygen fugacity during Earth accretion. *Geochim Cosmochim Acta* 72:574–589
- Dobson DP (2000) ⁵⁷Fe and Co tracer diffusion in liquid Fe–FeS at 2 and 5 GPa. *Phys Earth Planet Int* 120:137–144
- Dobson DP (2002) Self-diffusion in liquid Fe at high pressure. *Phys Earth Planet Int* 130:271–284
- Dobson DP, Wiedenbeck M (2002) Fe- and C-self-diffusion in liquid Fe₃C to 15 GPa. *Geophys Res Lett*. <https://doi.org/10.1029/2002GL015536>
- Fedotenko T, Khandarkhaeva S, Dubrovinsky L, Glazyrin K, Sedmak P, Dubrovinskaia N (2021) Synthesis and compressibility of novel nickel carbide at pressures of the Earth's outer core. *Minerals* 11:516. <https://doi.org/10.3390/min11050516>
- Fischer RA, Nakajima Y, Campbell AJ, Frost DJ, Harries D, Langenhorst F, Miyajima N, Pollok K, Rubie DC (2015) High pressure metal-silicate partitioning of Ni, Co, V, Cr, Si and O. *Geochim Cosmochim Acta* 167:177–194
- Fonseca ROC, Mallmann G, O'Neill HSC, Campbell IH, Laurenz V (2011) Solubility of Os and Ir in sulfide melt: Implications for Re/Os fractionation during mantle melting. *Earth Planet Sci Lett* 311:399–350
- Gubbins D, Davies CJ (2013) The stratified layer at the core–mantle boundary caused by barodiffusion of oxygen, sulfur and silicon. *Phys Earth Planet Inter* 215:21–28
- Harrison WA (1980) Electronic structure and the properties of solids: The physics of the chemical bond. Freeman, San Francisco
- Hirose K, Wood B, Vočadlo V (2021) Light elements in the Earth's core. *Nature Rev Earth Environ*. <https://doi.org/10.1038/s43017-021-00203-6>
- Jeanloz R (1990) The nature of the Earth's core. *Ann Rev Earth Planet Sci* 18:357–386
- Keehan E, Karlsson L, Andrén HO (2006) Influence of carbon, manganese and nickel on microstructure and properties of strong steel weld metal. Part 1: effect of nickel content. *Sci Technol Weld Joi* 11:1–8
- Knittle E, Jeanloz R (1991) Earth's core-mantle boundary: results of experiments at high pressure and temperatures. *Science* 251(5000):1438–1443
- Knowles PR (1987) Design of structural steelwork, 2nd edn. Taylor & Francis, Germantown, pp 1–15
- Korell J-A, French M, Steinle-Neumann G, Redmer R (2019) Paramagnetic-to-diamagnetic transition in dense liquid iron and its influence on electronic transport properties. *Phys Rev Lett* 122:086601
- Kresse G, Furthmüller J (1996) Efficient iterative schemes for ab initio total-energy calculations using a plane-wave basis set. *Phys Rev B* 54:11169
- Kresse G, Joubert J (1999) From ultrasoft pseudopotentials to the projector augmented-wave method. *Phys Rev B* 59:1758
- Liu WJ, Brimacombe JK, Hawbolt EB (1991) Influence of composition on the diffusivity of carbon in steels–I. Non-alloyed austenite. *Acta Metallurgica Et Materialia* 39(10):2373–2380
- Luo S-N, Ahrens TJ, Çağın T, Strachan A, Goddard WA III, Swift DC (2003) Maximum superheating and undercooling: systematics, molecular dynamics simulations, and dynamics experiments. *Phys Rev B* 68:134206
- Mashino I, Miozzi F, Hirose K, Morard G, Sinmyo R (2019) Melting experiments on the Fe–C binary system up to 255 GPa: constraints on the carbon content in the Earth's core. *Earth Planet Sci Lett* 515:135–144
- Nakajima Y, Takahashi E, Suzuki T, Funakoshi K-I (2009) “Carbon in the core” revisited. *Phys Earth Planet Int* 174:202–211
- Ohmura S, Tsuchiya T, Shimojo F (2020) Structures of liquid–light-element mixtures under high pressure. *Phys Status Solidi B*. <https://doi.org/10.1002/pssb.202000098>

- Perdew JP, Burke K, Wang Y (1996) Generalized gradient approximation for the exchange-correlation hole of a many-electron system. *Phys Rev B* 54:533–539
- Posner ES, Steinle-Neumann G (2019) Mass transport and structural properties of binary liquid iron alloys at high pressure. *Geochem Geophys Geosyst* 20:3556–3568
- Posner ES, Rubie DC, Frost DJ, Steinle-Neumann G (2017a) Experimental determination of oxygen diffusion in liquid iron at high pressure. *Earth Planet Sci Lett* 464:116–123
- Posner ES, Rubie DC, Frost DJ, Vlček V, Steinle-Neumann G (2017b) High P-T experiments and first principles calculations of the diffusion of Si and Cr in liquid iron. *Geochim Cosmochim Acta* 203:323–342
- Posner ES, Steinle-Neumann G, Vlček V, Rubie DC (2017c) Structural changes and anomalous self-diffusion of oxygen in liquid iron at high pressure. *Geophys Res Lett* 44:3526–3534
- Rebaza AM, Posner ES, Thielmann M, Rubie DC, Steinle-Neumann G (2021) Experimental determination of carbon diffusion in liquid iron at high pressure. *Am Mineral*. <https://doi.org/10.2138/am-2021-7644>
- Rubie DC, Melosh HJ, Reid JE, Liebske C, Righter K (2003) Mechanisms of metal-silicate equilibration in the terrestrial magma ocean. *Earth Planet Sci Lett* 205:239–255
- Rubie DC, Jacobson SA, Morbidelli A, O'Brien DP, Young ED, de Vries J, Nimmo F, Palme H, Frost DJ (2015) Accretion and differentiation of the terrestrial planets with implications for the compositions of early-formed Solar System bodies and accretion of water. *Icarus* 248:89–108
- Tsymbulov LB, Tsemekhman LSh (2001) Solubility of carbon in sulfide melts of the system Fe–Ni–S. *Inorgan Synth Indust Inorgan Chem* 74:925–929
- Vander Voort GF (2001) Metallography of iron meteorites. *Adv Mat Proc* 159(2):37–41
- Wang J, Chen B, Williams Q, Manghnani MH (2019) Short- and intermediate-range structure and dynamics of Fe–Ni–C liquid under compression. *Frontier Earth Sci*. <https://doi.org/10.3389/feart.2019.00258>
- Watanabe M, Adachi M, Fukuyama H (2016) Densities of Fe–Ni melts and thermodynamic correlations. *J Mater Sci* 51:3303–3310
- Wells AF (1984) *Structural inorganic chemistry*, 5th edn. Clarendon Press, Oxford, p 1288
- Wood BJ (1993) Carbon in the core. *Earth Planet Sci Lett* 117:593–607

Publisher's Note Springer Nature remains neutral with regard to jurisdictional claims in published maps and institutional affiliations.